

# Uniaxial static mechanical properties of regular, irregular and random additively manufactured cellular materials: Nominal vs. real geometry



Sunil Raghavendra <sup>a,\*</sup>, Alberto Molinari <sup>a</sup>, Michele Dallago <sup>a</sup>, Gianluca Zappini <sup>b</sup>, Filippo Zanini <sup>c</sup>,  
Simone Carmignato <sup>c</sup>, Matteo Benedetti <sup>a</sup>

<sup>a</sup> Department of Industrial Engineering, University of Trento, Via Sommarive 9, 38123 Trento, Italy

<sup>b</sup> Lincotek Medical, Via Al Dos de la Roda, 60, 38057 Ciré-Pergine, Trento, Italy

<sup>c</sup> Department of Management and Engineering, University of Padova, Stradella San Nicola 3, 36100 Vicenza, Italy

## ARTICLE INFO

### Keywords:

Cellular structure  
Laser based powder bed fusion  
X-ray computed tomography  
Trabecular  
Titanium alloys

## ABSTRACT

The present work investigates cellular materials that can be potentially used as a replacement of solid implants owing to their mechanical properties and biocompatibility. More specifically, titanium alloy (Ti6Al4V) cellular materials of three different topologies were considered to study the effect of the degree of irregularity. Cubic regular, cubic irregular and trabecular structures were manufactured using Laser based powder bed fusion (LB-PBF) process. The LB-PBF process had an impact on the strut thickness of the samples. Samples were subjected to micro computed tomography to understand the geometrical deviations and to use the actual geometry for finite element analysis. Mechanical properties such as Young's modulus and strength were derived from compression and tensile testing. The results indicate that the Young's modulus was between 6 and 17 GPa, which were closer to the values of human cortical bone. The finite element analysis results showed a good correlation with the tensile test results as well. Furthermore, Gibson-Ashby model is used to study the effect of cell topology on the structural behavior. The model indicated that the misalignment of nodes of cubic regular structures to form irregular structure, transformed the stretching dominated behavior of cubic structures to bending dominated behavior like trabecular structures. Finally, the regular structures appeared to be much more prone to catastrophic failure than irregular and trabecular structures. Both visual observation of experimental testing and FE analysis explained this difference as result of different modes and zones of failures.

## 1. Introduction

Additive manufacturing (AM) allows three-dimensional (3D) parts production through layer-by-layer addition of material starting from a sliced 3D CAD file. AM has the ability to manufacture products ranging from micro to macro scale irrespective of the complex geometries. A range of materials from polymers to metals can be used in the AM process [1]. Powder bed systems, powder feed systems and wire feed systems are the basic methodologies used in the additive manufacturing of metals. In particular, powder bed fusion systems employing electron beam (EB-PBF) or laser beam (LB-PBF) previously known as electron beam melting (EBM) and selective laser melting (SLM) have been used extensively [2,3]. In this current study LB-PBF process [4–6] was used to manufacture the specimens. The LB-PBF process is commonly used for the fabrication of cellular materials, which attracted the interest of the scientific community thanks to their light weight and high specific strength. Cellular materials can be divided into two types according to the topology, stochastic or periodic. Foams are stochastic

cellular materials whereas lattices are periodic cellular materials with a repeating unit cell along all the three directions [7]. Depending on the morphology of cellular materials, they are extensively used in packaging industry, automotive, aerospace and biomedical applications. Lattices are used in load bearing applications as well since their properties can be tailored depending on the loading direction [8]. They are characterized by the type of unit cell, strut thickness and pore size. Lattices are either bending dominated or stretching dominated depending on the deformation mechanism, which is defined by the cell topology. Bending dominated lattices are more compliant, while stretching dominated are stiff and designed for axial loading conditions [9,10].

Titanium alloy (Ti6Al4V) cellular materials are widely used in biomedical implants due to their good corrosion resistance, high specific strength and stiffness [11–13]. Thanks to the AM technologies, the properties of these implants can be tailored to match the stiffness of bone (3–20 GPa) to avoid stress shielding [14]. The current study focuses on Ti6Al4V lattice materials manufactured by LB-PBF process. Various studies have been carried out to understand the mechanical and

\* Corresponding author.

E-mail address: [sunil.raghavendra@unitn.it](mailto:sunil.raghavendra@unitn.it) (S. Raghavendra).

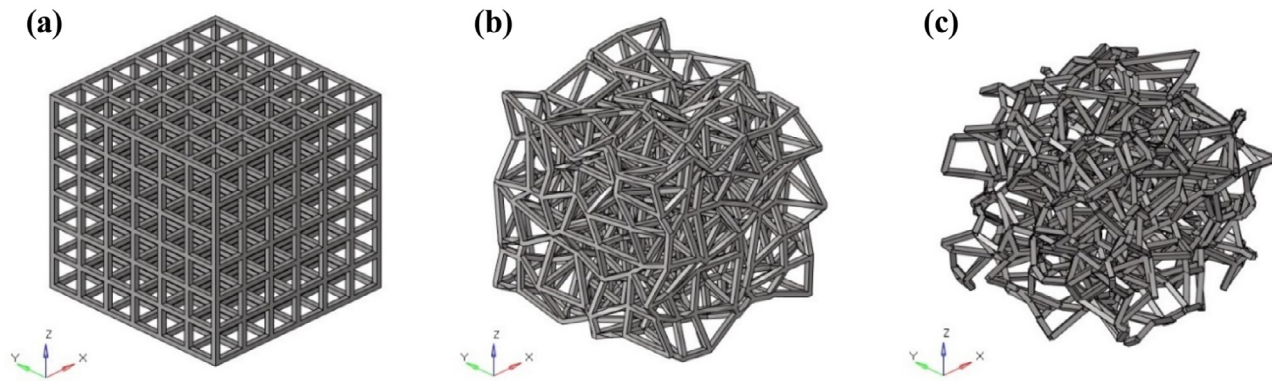


**Fig. 1.** Schematic representing (a) cubic regular, (b) cubic irregular and (c) trabecular structures.

metallurgical behavior of such materials fabricated using AM process. Their mechanical response is highly influenced by the cell topology and relative density. Various cell topologies such as cubic, diamond, rhombic dodecahedron, BCC, tetrahedron have been studied under static and fatigue loading [15–17]. The recent studies also include structures with graded porosity [18] and triply periodic minimum surface (TPMS) based gyroid structures [19,20]. These studies concluded that an increase in the relative density increases the stiffness and the strength of the structure, while the cell topology influences the deformation behavior. This behavior can be mathematically modeled using the Gibson-Ashby power law [21].

Along with the above-mentioned parameters, microstructure, process parameters and defects also influence the properties of bulk as well as lattice materials manufactured through LB-PBF. Zhang et al. studied the transformation of  $\alpha$ -martensitic phase to a stable  $\alpha+\beta$  phase in Ti6Al4V alloys using heat treatment at different temperatures [22]. Other processes such as hot-isostatic pressing, shot peening and electro-polishing have a positive effect on the internal porosity, static and dynamic behavior [23,24]. LB-PBF process parameter such as laser power, scanning distance, and scanning speed influence the building quality and mechanical behavior of cellular materials [25]. Qiu et al. [26], for example, concluded that increasing the laser power increased the strut thickness, surface roughness and internal porosity. Vertical struts are printed with least internal porosity and strut defects, while inclined and horizontal struts have the porosity in the bottom part of the struts [27]. Strut defects such as waviness, eccentricity, and increased thickness influence the mechanical response under static and fatigue loads [28,29].

To study the above-mentioned defects, micro X-ray computer tomography ( $\mu$ CT) is being used extensively for AM foams and cellular materials, thanks to the unique capability of  $\mu$ CT to analyze both external and internal geometries and features in a non-destructive manner [30]. du Plessis [31] conducted an extensive study on the effect of process parameters and evaluated the bulk samples using  $\mu$ CT. Strut defects, geometrical deviations, internal porosities and damage modes [32] have been analyzed for cellular materials as well as bulk materials [33,34]. Lozanovski et.al. [35] used tomography to replicate strut defects from LB-PBF using a new modeling technique. Van Bael et al. [36] used  $\mu$ CT in a loop to control the geometry of the Ti6Al4V structures, the mismatch in the pore size was reduced from 45% to 5%. Finite element (FE) models generated from  $\mu$ CT scans have been subjected to in-situ loading [37] or using analyses software to replicate the experimental results. These studies are mainly focused on the deformation behavior and localization of stresses due to defects for regular lattice structures and foams [37–39]. Most of the studies in cellular materials involve their characterization using compression and fatigue loads. However, failure studies of unexpected fracture of joint prostheses revealed that excess activity, higher weight in patients, improper positioning and loosening

of implants induce tensile stress in prostheses [40,41]. Also a previous study conducted by us indicated that the specimens showed an asymmetric behavior due to inclination in load during compression test, while tensile tests allowed for better alignment of the specimen along the loading axis leading to an accurate estimation of stiffness [42]. Therefore, there is need to investigate the properties of cellular materials under tensile loading along with compression and fatigue loads.

The main focus of this work is to study the less explored loading condition, viz. uniaxial tension, along with more commonly investigated uniaxial compression loading. The study involves three different cell topologies; cubic regular, cubic irregular (skewed junctions of cubic structures) and trabecular (random structure resembling the architecture of natural trabecular bone) manufactured using LB-PBF process are considered. All the samples had the same designed strut thickness and pore size. They were subjected to compression loading using cylindrical specimens, tensile tests were carried out on specifically designed specimens with solid grip ends under monotonic and cyclic loading conditions. Cyclic loading was used to investigate the effect of stabilization in cellular materials. Specimens were investigated using  $\mu$ CT for morphological deviations from the as-designed structures due to LB-PBF process. Furthermore, finite element analysis is carried out for as-designed structures from initial CAD and a part of the as-built structures extracted from  $\mu$ CT reconstructed models. The FE analysis was carried out only for tensile loading in elastic-plastic region. The results from the FE models are compared with the experimental data to obtain a clear understanding of the difference in the as-designed and as-built structure.

## 2. Materials and methods

This section provides details on the LB-PBF process parameters, unit cell topologies, experimental procedure, and conversion of STL files to FE models.

### 2.1. Manufacturing and specimen design

Three different unit cell topologies were studied; Cubic regular (Cr), Cubic irregular (Ci) and Trabecular (Tb) structures as shown in Fig. 1. They were designed with a nominal (i.e. as-designed) strut thickness of 200  $\mu$ m and an average pore size of 1500  $\mu$ m. Pore size is defined as the diameter of the sphere that can be inscribed in between the struts. The STL files of these structures were generated using the materialize software MAGICS 21.1<sup>®</sup> by the manufacturer. Cubic regular structures had square shaped unit cells repeated in all the three spatial directions (x, y and z), cubic irregular structures were formed by misaligning the junctions of cubic regular structures using an algorithm and trabecular structures were designed to resemble trabecular bone. The number of struts per junction is 6 for cubic regular and cubic irregular. For trabecular structures, the number of struts per junction vary between 4 and 6

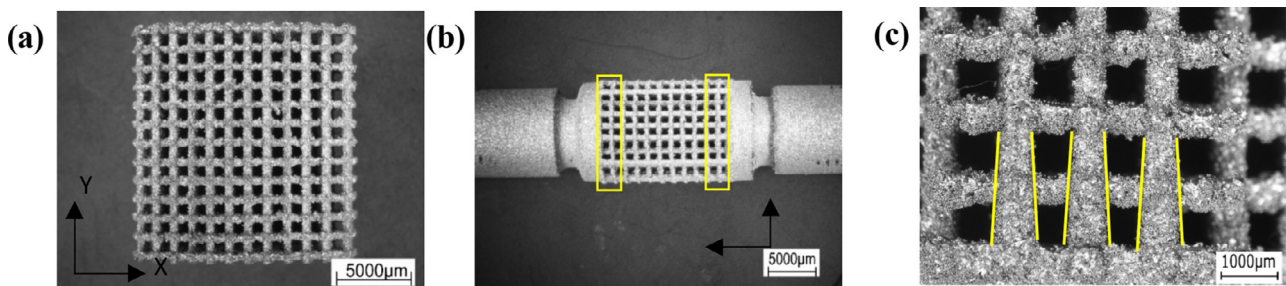


**Fig. 2.** (a) Compression testing sample, (b) tensile testing samples with grips and (c) transition in tensile samples.

struts. In cubic regular structures, the struts are along X,Y and Z directions. For cubic irregular, the struts are along X,Y and Z directions but with a slight inclination due to misalignment of junctions and for trabecular structures, the struts are in all the directions forming a random arrangement. The presence of 4–6 struts in random directions increases the density at the junctions, moreover at some junctions the struts overlap further increasing the density and decreasing the porosity. These STL files were used as input for the LB-PBF process.

Ti6Al4V cellular materials were manufactured using LB-PBF process at Lincotek Medical facility, Italy. A biomedical grade Ti6Al4V powder with particle size in the range 15–45  $\mu\text{m}$  was used. An EOS machine with a laser power of 400 W and a layer thickness of 60  $\mu\text{m}$  was used. The produced samples were subjected to heat treatment process according to the company standards to eliminate residual stresses and to transform the  $\alpha$ -martensitic as-built microstructure to a more stable  $\alpha+\beta$  lamellar structure [42]. Detailed parameters of the manufacturing process have not been disclosed by the manufacturer and are confidential.

Two sets of samples containing five specimens each were produced for all the topologies. The first set of samples had a cylindrical geometry as shown in Fig. 2(a), with a diameter of  $\sim 15$  mm (XZ plane) and length of 16 mm (Y-direction). These specimens were used for porosity calculations and compression test. The second set of specimens were specifically designed for tensile testing as shown in Fig. 2(b). The cellular part of the specimen consisted of gradual transition at the ends reaching a maximum thickness of  $\sim 1.8$  times the nominal strut thickness value as shown in Fig. 2(c). The transition is used to avoid stress concentration between the cellular and solid part of the specimen. The cellular part of the structure is used to calculate the porosity and the displacement during the tensile test. A minimum of 8–10 unit cells were maintained in all the directions for the specimens.

## 2.2. Experimental procedure

This section gives the detailed procedure followed to measure the porosity and calculation of mechanical properties.

The porosity content was calculated on both compression and tensile manufactured specimens mentioned in Section 2.1, using dry weight method. Five specimens in each configuration were weighed and the density of these specimens was then calculated using the measured mass and volume. To obtain the relative density of the samples, the density of the cellular structure is divided by the bulk density of Ti6Al4V ( $4.42 \text{ g/cm}^3$ ). The porosity is calculated using the method proposed in a previous work by Raghavendra et al. [42].

Compression and tensile test were carried out under monotonic and cyclic loading conditions. ISO 13314:2011 was followed for compression test, and tensile test specimens were subjected to standard tensile testing using an Instron universal testing machine. The tests were conducted at room temperature at a crosshead speed of 1 mm/min, 1 kHz of data sampling frequency, and samples were loaded along Y-direction. Displacement was measured using a linear variable displacement transducer (LVDT) and an extensometer for compression and tensile test, respectively. Young's modulus, offset yield strength and

maximum strength were calculated using stress-strain curves from the monotonic test. According to ISO 13314:2011, to calculate the Young's modulus using the unloading test, a cyclic test was carried out. The cyclic test was carried out by loading and unloading the specimen between 20% and 70% of the yield load calculated from the monotonic test to obtain a hysteresis. The subsequent loading and unloading of the specimen were carried out for 5 cycles to obtain stability. One specimen was tested under monotonic load and four specimens were tested under cyclic loading.

## 2.3. X-ray computed tomography

One compression test sample for each configuration was subjected to  $\mu\text{CT}$  scanning using a metrological  $\mu\text{CT}$  system (Nikon Metrology MCT225), characterized by micro-focus X-ray tube, 16-bit detector with  $2000 \times 2000$  pixels, high-precision linear guideways and controlled cabinet temperature at  $20 \pm 0.5^\circ\text{C}$ . The use of a metrological system was preferred to conventional  $\mu\text{CT}$  scanners in order to measure the samples with higher dimensional accuracy [43]. 3D voxel-based models of the scanned objects were reconstructed with voxel size equal to  $8.3 \mu\text{m}$ . After the reconstruction and the determination of the surface by means of the local-adaptive algorithm implemented in the analysis and visualization software VG Studio MAX 3.2 (Volume Graphics GmbH, Germany), a high-density point cloud of the surface was extracted for FE modeling (see Section 2.4). The voxel-based models were also used to compute and visualize the variation in the strut thickness values from the as-designed values, using the 'Wall-thickness analysis' module of VG Studio MAX 3.2.

## 2.4. Finite element modeling

The finite element analysis was carried out for as-designed structures obtained from the initial CAD models. For as-built structures, the point clouds generated from  $\mu\text{CT}$  data were used to generate STL files. The STL files were then converted to 3D solid mesh models using the 'shrink wrap' option in Hypermesh<sup>®</sup> (Altair), as explained in Section 2.4.1. FE analysis under elastic-plastic regime under tensile loading condition was performed as explained in Section 2.4.2.

### 2.4.1. Conversion of STL to solid mesh

To convert the point clouds extracted from the CT scans to 3D solid mesh files, MeshLab<sup>®</sup> and Hypermesh<sup>®</sup> (Altair) were used. Initially, the highly dense point cloud was subjected to down sampling using MeshLab. This point was converted into a surface mesh (STL file) using triangular elements. Down sampling was carefully chosen as to not lose the most relevant geometrical details. The 'shrink wrap option' (tight wrap) of Hypermesh was used to obtain the 3D mesh file starting from the STL file. Fig. 3 shows the step-by-step transformation of point cloud into 3D mesh. Since the analysis of the complete model is not feasible due to the computational constraints, representative volume elements(RVE) models shown in Fig. 4 was used. The size of the RVE for cubic regular

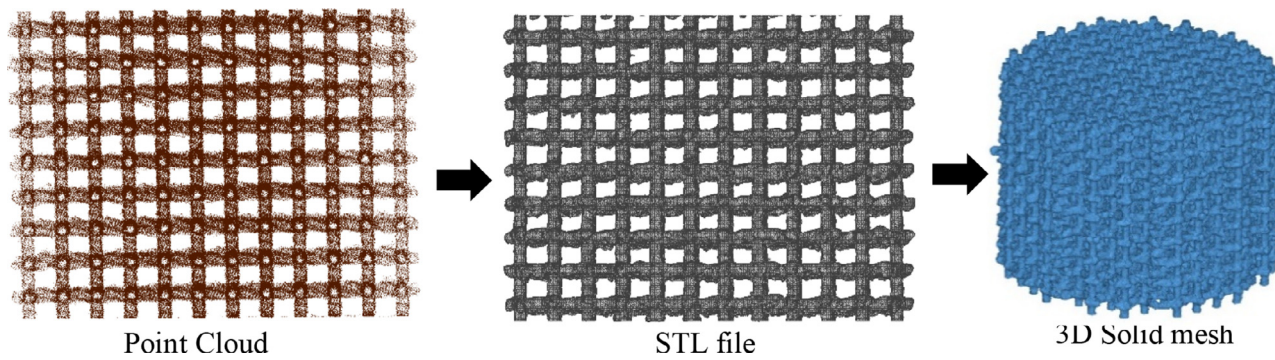


**Fig. 3.** Conversion of point could to 3D solid mesh.

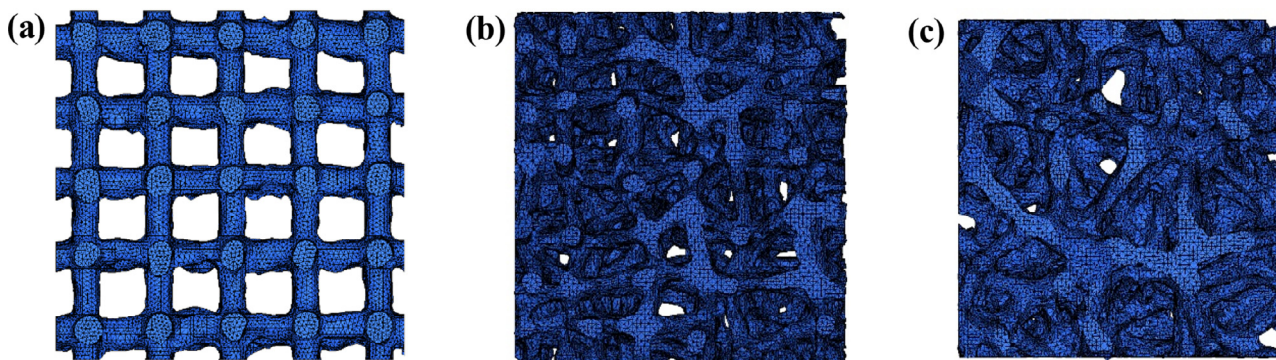


**Fig. 4.** 3D FE models from point clouds: (a) cubic regular, (b) cubic irregular and (c) trabecular.

structures was selected to have 5 unit cells in each direction [28,44], while the size of the RVE for cubic irregular and trabecular was from the literature of foam based structures [45,46]. The RVE was selected to have at least 4–6 junctions in all the directions. The size of the RVE considered for the study was also limited by the computational limitations of the computer for the elastic-plastic analysis. For analysis of as-designed CAD structure, full scale STL file of tensile sample was converted into 3D CAD model. 10-noded tetrahedron elements with the element size ranging from 20 to 80  $\mu\text{m}$  were used for 3D meshing depending on the convergence analysis and the computational capacity of the computer. The number of elements in the considered FE models (both RVE and full scale as-designed CAD) vary between from 800,000 to 1,500,000 depending on the model.

#### 2.4.2. Elastic-plastic loading

To replicate the mechanical test, FE analysis was carried out on the  $\mu\text{CT}$  reconstructed models, under tensile load for monotonic conditions. 125-unit cells were considered for cubic regular samples, while for irregular cubic and trabecular structures RVE models were used. A displacement-based analysis was carried out by fixing the bottom surface in all the directions and lateral displacements was applied on the top surface. Displacement values were obtained from the experiments (until yielding of the specimens). The stress was calculated by dividing the reaction to the applied displacement and the nominal area of the FE model. Multilinear isotropic material model (MISO) in ANSYS<sup>®</sup> was used as the material input for FE analysis. The elastic and plastic properties required from the material modeling was obtained from the tensile testing of the bulk specimen manufactured using the same LB-PBF process. A Young's modulus of 109 GPa and the plastic region from the MISO curve was obtained from the stress-strain curves are provided in the following reference [28].

## 3. Results and discussion

### 3.1. Microstructure

The microstructure of AM manufactured Ti6Al4V alloy consists of acicular  $\alpha'$  martensite in the as-built condition. This is formed due to the rapid cooling during the LB-PBF process and the size of these martensite depends on the LB-PBF process parameters [47]. The heat treatment process on the as-built structures transforms of this  $\alpha'$  martensitic phase to a more stable needle like  $\alpha+\beta$  lamellar phase [24] as shown in Fig. 5. The microstructure on the side parallel to the printing direction shown in Fig. 5(a), the  $\alpha+\beta$  grains are thicker and oriented along the printing direction in certain locations. The microstructure was fine and completely random in the plane perpendicular to printing directions.

### 3.2. Porosity and morphological analysis

The  $\mu\text{CT}$  analysis of the samples was used to obtain quantitative information on strut thickness, strut variations, disconnected struts, and overall porosity. Fig. 6(a) shows an example of strut thickness variation in the lateral plane of the scanned cubic regular sample. It can be seen that the vertical struts have uniform thickness compared to horizontal struts, which exhibit strut waviness that include varying thickness and center offset. The cause of high strut waviness in horizontal struts is related to the fact that during the LB-PBF process the first few layers of horizontal struts are built on loosen powder and lack support: these loosen particles below the first layer is melted partially by the laser leading to an excess of molten material on unsupported surfaces. Similar results were obtained also for the other cross-sections (both lateral and transverse planes) and for all the analyzed samples. Fig. 6(b-d) indicates the distribution of the strut thickness values in the all the samples. Maximum surface area has a strut thickness in the range of 300–400  $\mu\text{m}$ , deviating from the designed strut thickness value of 200  $\mu\text{m}$ .

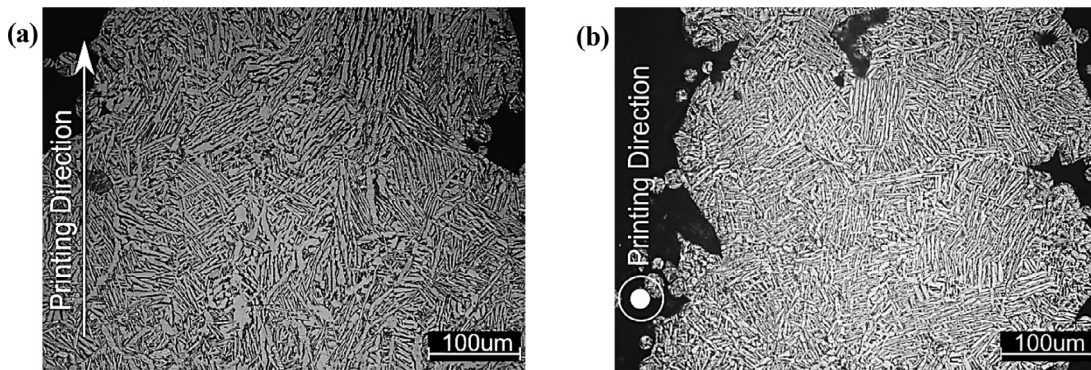


**Fig. 5.** Microstructure of cellular materials after heat treatment: (a) parallel to the printing direction and (b) perpendicular to the printing direction.

**Table 1**  
Summary of porosity of structures.

Sample	Designed porosity (%)		Measured porosity (%) <i>Dry weight method</i>		$\mu$ CT model cellular porosity (%)
	Compression sample	Tensile sample	Compression sample	Tensile sample	
Cubic Regular	90	87	76 ± 0.15	70 ± 0.34	74
Cubic Irregular	88	85	71 ± 0.21	65 ± 0.20	70
Trabecular	85	81	70 ± 0.32	69 ± 0.24	73

The normalized center offset gives a direct correlation to the irregularities of the struts. Fig. 6(e) shows the overlapping between the as-designed struts and as-built struts. It is clearly visible that not only there was a thickness variation but also an offset in the center which led to waviness in the struts. The normalized offset was calculated by taking the difference in the center of the as-designed model and the as-built circumference and dividing it by the nominal thickness/CAD thickness. The struts in all the structures were categorized as horizontal, vertical and inclined to printing plane. The plot shown in Fig. 6(f) indicates that horizontal struts (parallel to printing plane) had the highest normalized offset with a wide distribution, confirming the effect of unsupported surfaces. Vertical struts (perpendicular to printing plane) had the normalized offset in the range of 0–20% and a narrow distribution. The inclined struts had the offset and the distribution between the horizontal and vertical values. Similar results for vertical and horizontal struts have been discussed by Dallago et al., [29].

The porosity values tabulated in Table 1 are obtained from two different methods; dry weight method and  $\mu$ CT as discussed in Sections 2.2 and 2.3 respectively. A considerable difference is seen in the designed and measured porosity of the samples. A deviation in the range of 15–23% was observed when comparing the designed porosity and porosity from dry weight method. The deviation was slightly on the higher side for tensile samples compared to compression samples due to the presence of transition. As mentioned earlier, the increase in the thickness values proportionally decreases the porosity. Similar results of variation in thickness values from designed values were discussed by Parthasarathy et al., for samples manufactured using EBM process [49] and Dallago et al., for cubic samples manufactured using LB-PBF process [50]. LB-PBF process parameters such as laser power and layer thickness play a major role in the geometrical deviation of struts. Qiu et.al., concluded that increasing the laser power increased the strut thickness, while increasing the scanning speed decreased the strut thickness in AlSi10Mg cellular structures, thus varying the porosity of the samples [26].

### 3.3. Compression and tensile test

The stress-strain curves are as shown in Fig. 7. One specimen was tested in monotonic loading and four specimens under cyclic loading. The yield load from monotonic tests were used for cyclic loading as

discussed in Table 3. The samples were tested until a failure of struts were observed under monotonic load.

The tensile stress-strain curves are as shown in Fig. 7(a). It was observed that cubic regular structures failed drastically. Conversely, cubic irregular and trabecular structures undergo elongation even after an initial decrease in the stress due to strut failure. Additionally, the stress-strain curves of compression test are as shown in Fig. 7(c). The graphs indicate that the cubic regular structures do not exhibit any plateau region and fail at very low strain values of ~0.3. However, a clear plateau region was observed for cubic irregular and trabecular samples. The failure locations under compression are shown in Fig. 8. The failure of cubic regular samples is due to buckling of single row of struts. In cubic irregular structures the failure appears like a shear band, while in trabecular structures it leads to a non-simultaneous compaction of strut layers. These structures appear to be more resilient than cubic regular structures.

The cyclic test graphs are as shown in Fig. 7(b) and (d). According to Gibson et al. [21], the Young's modulus of the cellular structures shall be calculated from the unloading cycle. It was evident that there was a difference in slope between the first loading cycle and the next consecutive cycles. A perfect overlap of the curve was seen for cubic regular under tensile load. The compression test graphs shown in Fig. 7(d) suggest that the loading curve is not linear for any of the samples and a stability is reached from the unloading cycle. The modulus is obtained from the curve where the overlap is observed. The Young's modulus values tabulated in Table 2 clearly indicates the difference in the monotonic and cyclic Young's modulus. For cubic regular samples, the difference in Young's moduli measured in monotonic and cyclic is lower, for both compression and tensile. However, when comparing the monotonic and cyclic Young's moduli for cubic irregular and trabecular samples the following observations were made. Under compression load, the Young's modulus observed in monotonic test is approximately half of the Young's modulus observed in cyclic loading. Under tensile loading, the difference between the Young's moduli in monotonic and cyclic test was prominent but was not drastic. This indicates that the stabilization of the sample is achieved early in tensile test compared to compression test, where the stabilization is achieved after first unloading cycle. Therefore, Young's modulus from cyclic test is used in further discussion. When comparing the cyclic Young's modulus between and compression and tensile loading, approximately 27% increase in the modulus was observed in tensile test when compared to compression test

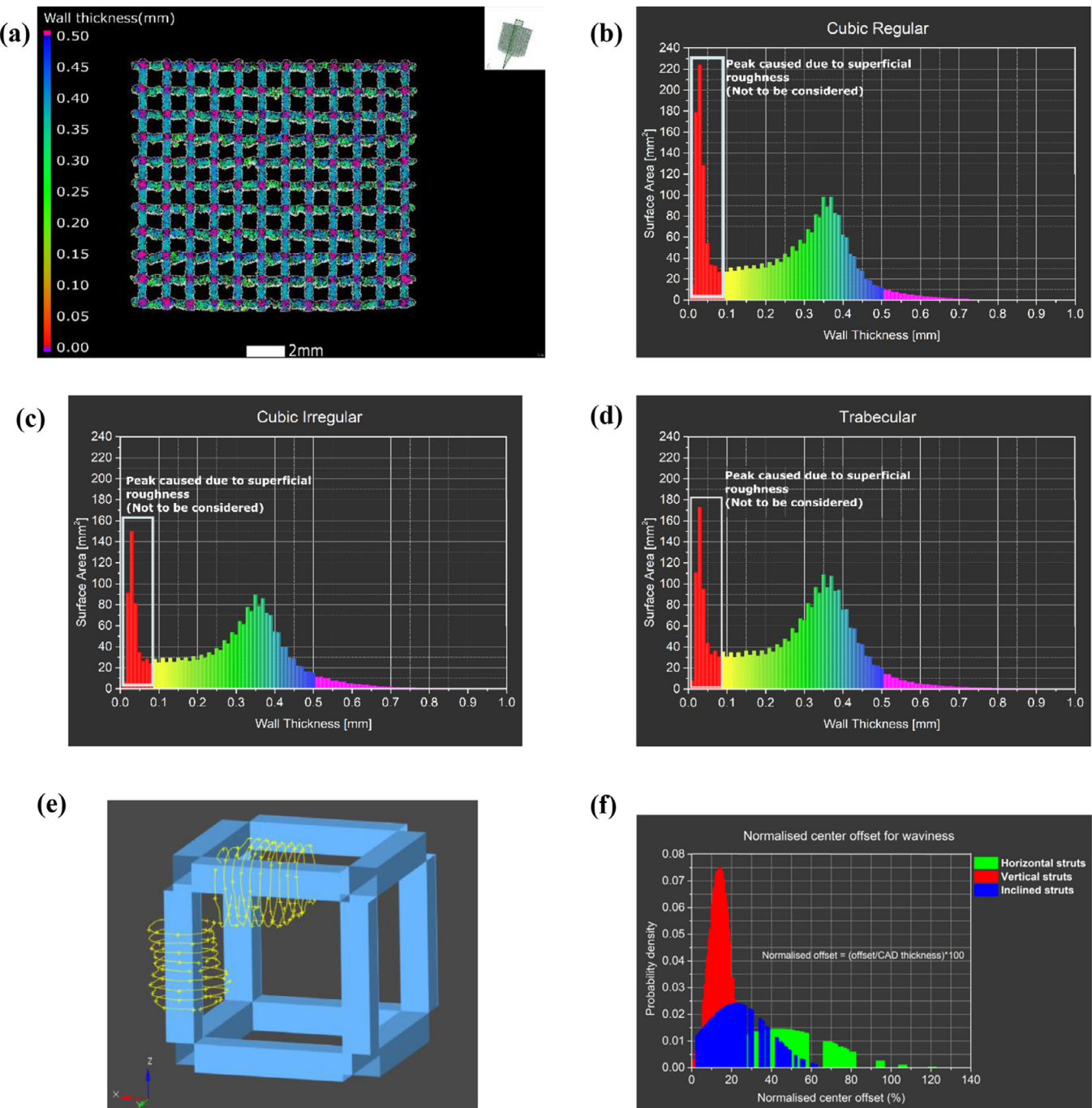


**Fig. 6.**  $\mu$ CT evaluation of thickness variation: (a) example of strut thickness variation shown on a cross-section of the scanned cubic regular sample; (b-d) strut thickness distribution in cubic regular, cubic irregular, trabecular structure, respectively (red peaks to the left are related to the complex topography of the surfaces as explained by Zanini et al. [48], and should not be considered); (e) strut cross-section circumferences overlapping as-designed CAD and (f) normalized center offset for different struts.

**Table 2**  
Summary of Young's modulus.

Sample	Porosity (%)		Tensile Young's modulus (GPa)		Compression Young's modulus (GPa)	
	Compression sample	Tensile sample	Monotonic	Cyclic	Monotonic	Cyclic
Cubic Regular	76 $\pm$ 0.15	70 $\pm$ 0.34	16.31	15.42 $\pm$ 0.17	13.43	11.29 $\pm$ 1.24
Cubic Irregular	71 $\pm$ 0.21	65 $\pm$ 0.20	11.82	9.61 $\pm$ 0.33	3.74	6.97 $\pm$ 0.66
Trabecular	70 $\pm$ 0.32	69 $\pm$ 0.24	7.34	6.61 $\pm$ 0.37	2.82	6.39 $\pm$ 0.39

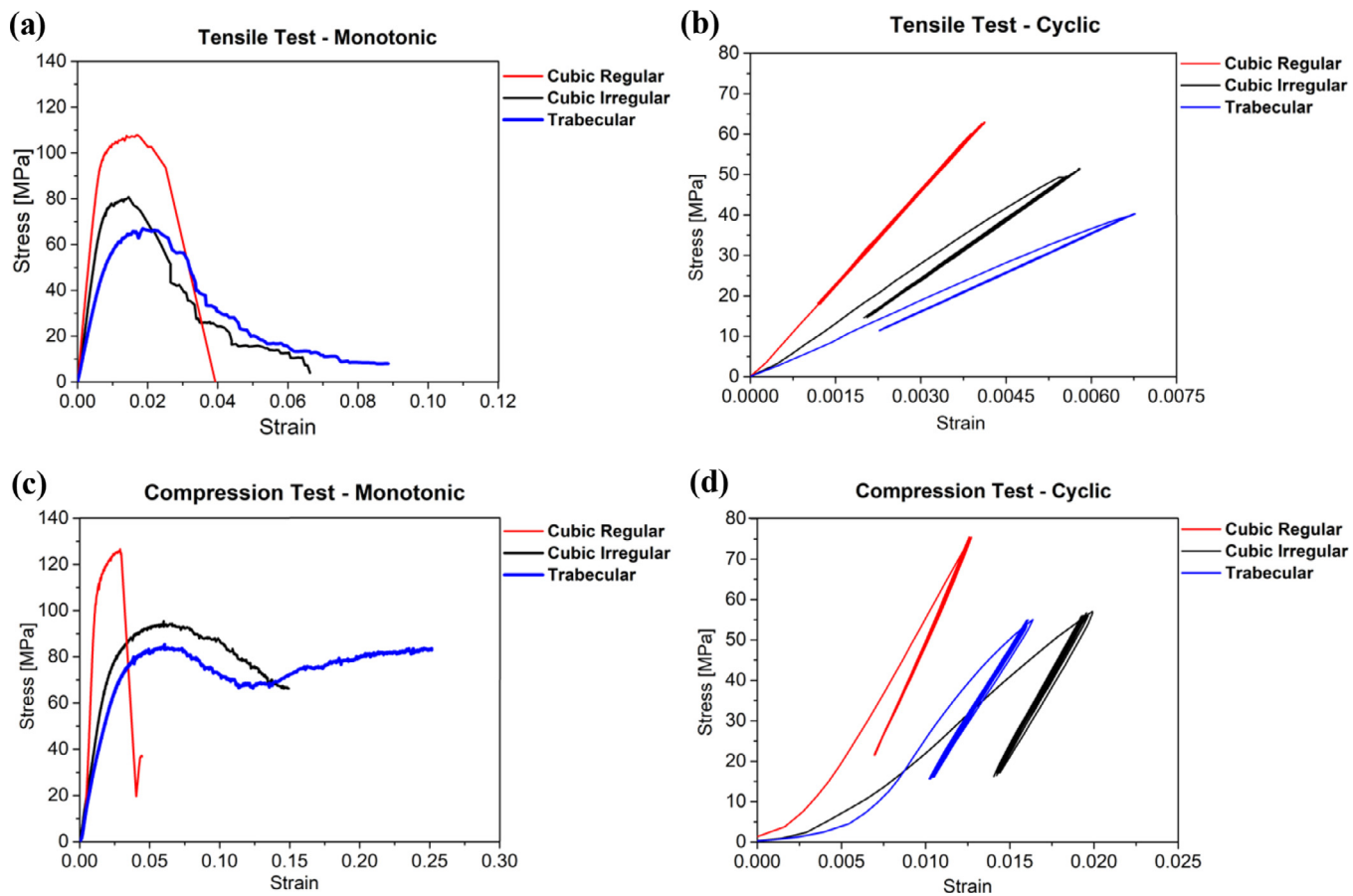


Fig. 7. Stress-strain curve (a), tensile monotonic, (b) tensile cyclic, (c) compression monotonic and (d) compression cyclic.

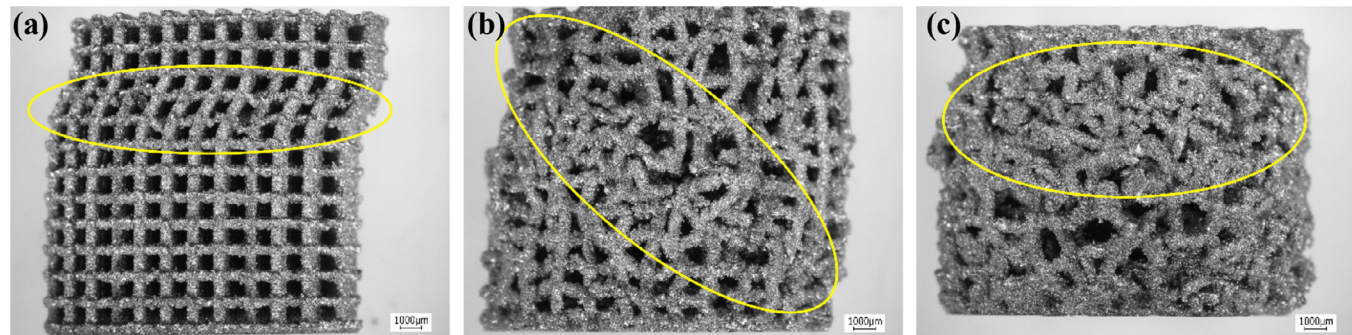


Fig. 8. Failure locations for (a) cubic regular, (b) cubic irregular and (c) trabecular.

**Table 3**  
Summary of strength values.

Sample	Porosity (%)		0.2% Offset yield strength (MPa)		Maximum strength (MPa)	
	Compression sample	Tensile sample	Tensile	Compression	Tensile	Compression
Cubic Regular	76 ± 0.15	70 ± 0.34	100	111	108	126
Cubic Irregular	71 ± 0.21	65 ± 0.20	76	71	81	95
Trabecular	70 ± 0.32	69 ± 0.24	56	55	68	85

for cubic regular and cubic irregular samples. However, this difference between compression and tensile cyclic Young's modulus was 3% for trabecular samples. This discrepancy is due to the presence of transition in tensile samples as explained before. Gibson-Ashby model is used to explain this difference in the next section.

The strength values from the monotonic tests are tabulated in Table 3. The 0.2% yield strength of the samples is similar under both

loading conditions, but the maximum strength was higher in compression compared to tensile loading. The reason is probably related to difference in the failure mechanism: In tensile loading, the failure is due to the elongation of struts and crack propagation while in compression it is due to the crushing or buckling depending on the cell topology [4]. Comparing the stress-strain curves of different topologies considered, the trabecular samples had the lowest strength and stiffness. How-

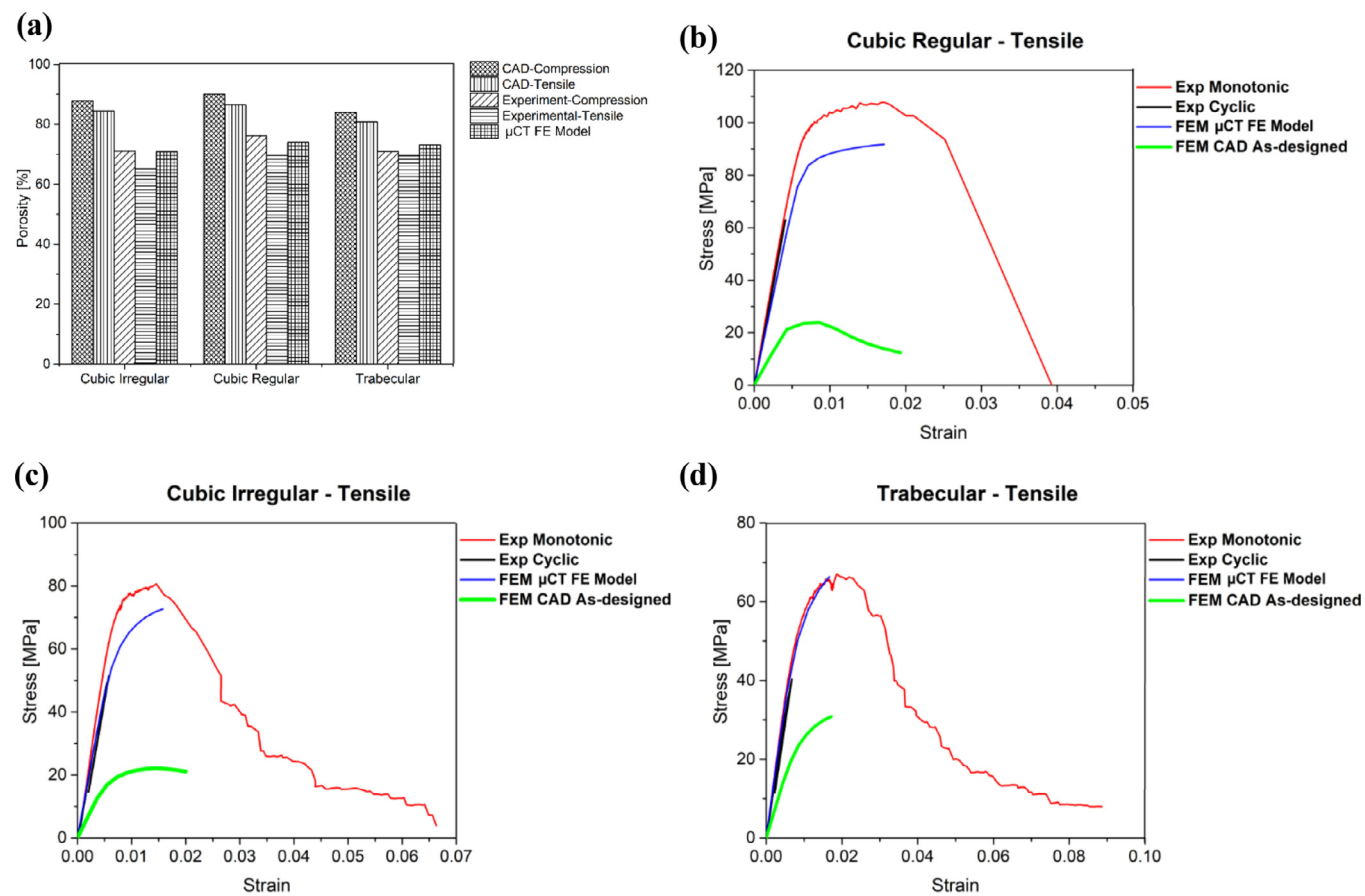


**Fig. 9.** (a) Porosity comparison of CAD as-designed, as-built and  $\mu$ CT models; stress-strain curves comparison of (b) cubic regular, (c) cubic irregular and (d) trabecular samples.

**Table 4**  
Comparison of Young's modulus.

Sample	Porosity			Tensile Young's modulus (GPa)			Error in Young's modulus(%)	
	CAD	Experimental	$\mu$ CT	CAD	Experimental		CAD	$\mu$ CT
					Monotonic	Cyclic		
Cubic Regular	87	$70 \pm 0.34$	74	5.00	16.31	$15.42 \pm 0.17$	13.56	68
Cubic Irregular	85	$65 \pm 0.20$	70	3.52	11.82	$9.61 \pm 0.33$	9.13	63
Trabecular	81	$69 \pm 0.24$	73	3.19	7.34	$6.61 \pm 0.37$	6.72	52

**Table 5**  
Comparison of 0.2% offset yield strength.

Sample	Porosity			Tensile – 0.2% offset yield strength (MPa)			Error in offset yield strength (%)	
	CAD	Experimental	$\mu$ CT	CAD	Experimental Monotonic	$\mu$ CT	CAD	$\mu$ CT
					Monotonic			
Cubic Regular	87	$70 \pm 0.34$	74	22	100	86	78	14
Cubic Irregular	85	$65 \pm 0.20$	70	20	76	60	74	21
Trabecular	81	$69 \pm 0.24$	73	26	56	55	54	2

ever, the longer plateau observed for trabecular specimens is beneficial, since the failure is not drastic under compression or under tension, when compared to the highly stiff cubic regular specimens. Nevertheless, a detailed study on the fatigue behavior of trabecular specimens and their comparison with the other unit cell configurations are under consideration for future studies.

The results indicate that the tensile testing has the least difference between the monotonic and cyclic test, therefore tensile test is more reliable in obtaining the Young's modulus. For this reason, the FE model obtained by  $\mu$ CT scan is subjected to tensile test and compared with the experimental data in the next section.

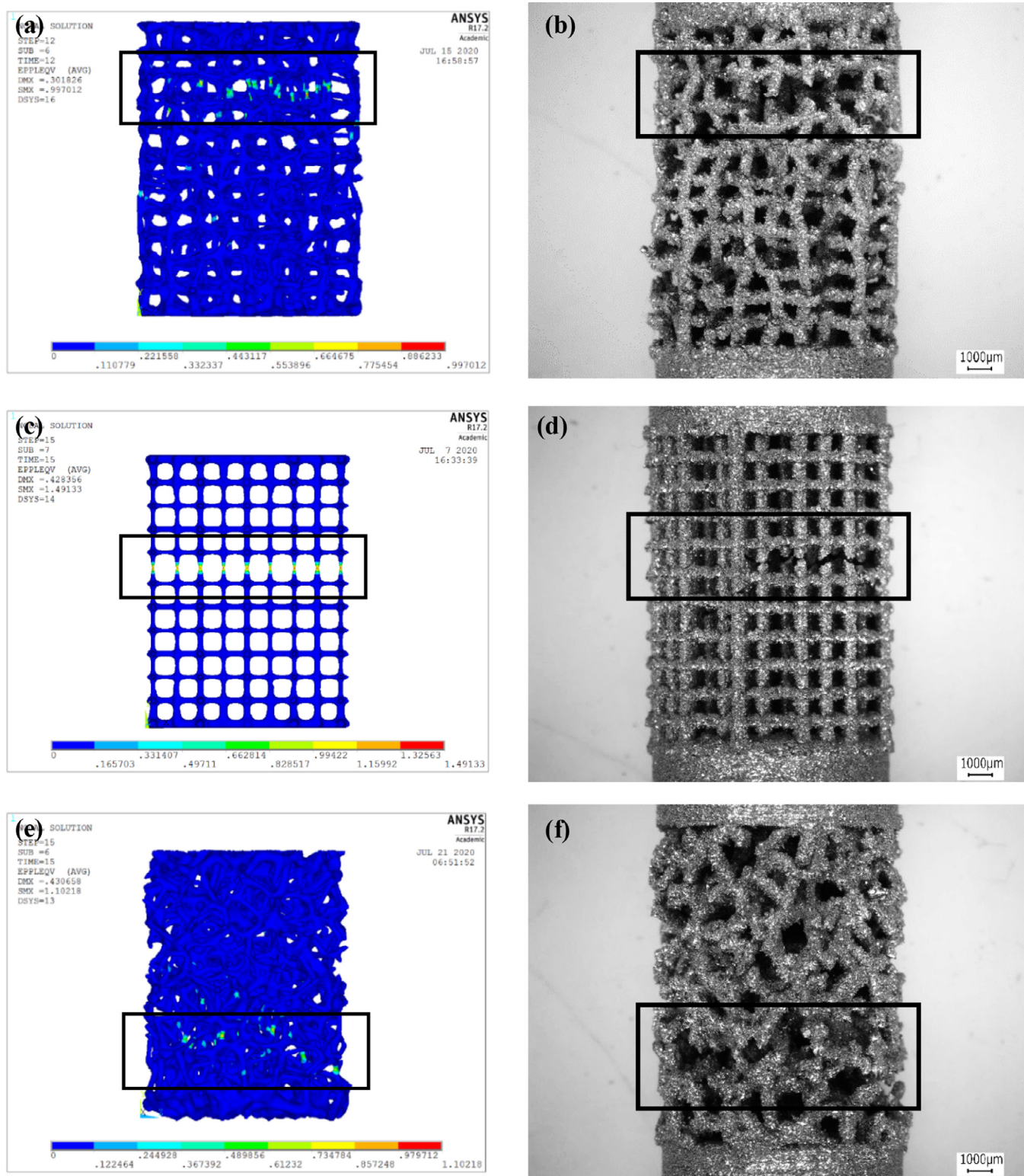


**Fig. 10.** Tensile loading fracture locations in FE analysis of CAD as-designed and experimental for (a, b) cubic irregular, (c, d) cubic regular and (e, f) trabecular samples.

#### 3.4. FE analysis: comparison of tensile experimental and μCT

The finite element modeling of the structures was done as mentioned in the [Section 2.3](#). Previous studies have shown that the porosity of cellular materials play a major role in mechanical properties [15,51]. Therefore, the porosity of the μCT models is compared with the as-designed

CAD models and experimental samples, shown in [Fig. 9\(a\)](#) and tabulated in [Tables 4](#) and [5](#). The graph indicates that the as-designed compression CAD model had the highest porosity followed by as-designed tensile CAD model. The same trend is seen for experimental samples. But this difference is the least for trabecular samples since the transition part in tensile samples was infused into the grips during the printing process.

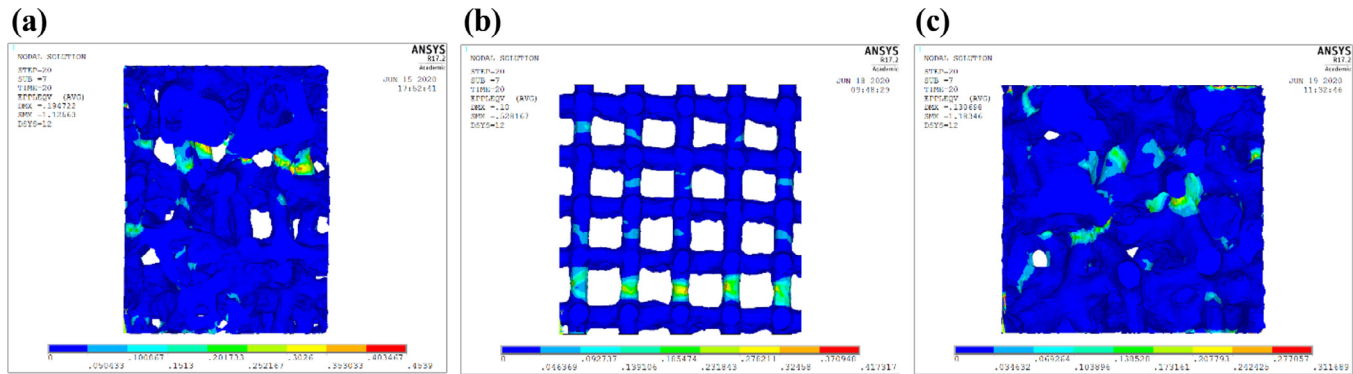


Fig. 11. Plastic strain in  $\mu$ CT models under tensile loading for (a) cubic irregular, (b) cubic regular and (c) trabecular samples.

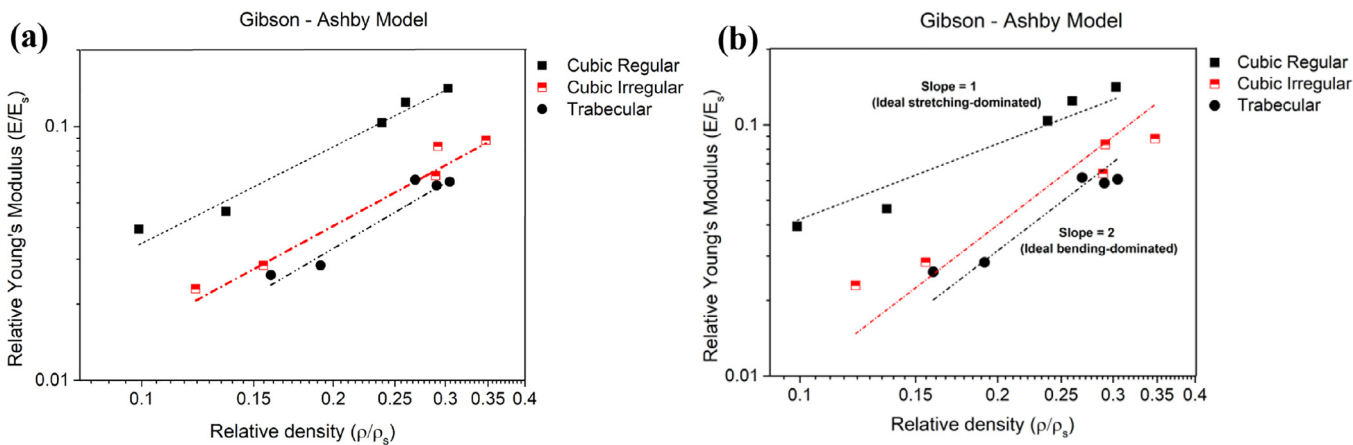


Fig. 12. (a) Relative Young's modulus with power law fitting (b) Relative Young's modulus in comparison with ideal stretching and bending dominated behavior using a linear fit with fixed slope values of 1 and 2.

Comparing the porosity of the as-designed CAD models with  $\mu$ CT models, the porosity of  $\mu$ CT models is higher than the as-designed tensile CAD model and lower than the as-designed compression CAD model.

As explained in the Section 2, the FE models from as-designed tensile CAD and  $\mu$ CT were subjected to only tensile loading until a point little beyond the yielding point obtained from the experiment. The stress-strain curve obtained from FE models is compared with the experimental curves as shown in Fig. 9. The Young's moduli of all the models are tabulated in Table 4, along with their respective porosity values. The results indicate a clear increase in the stiffness with decrease in the porosity. Comparing the experimental curves and the CAD as-designed curves, a considerable difference is observed. The 0.2% yield strength in experimental samples is between 60 and 100 MPa while in CAD as-designed structures it is in the range of 20–30 MPa as indicated in Table 5. When comparing the strength and stiffness values from experimental data and FE analysis of  $\mu$ CT (FEM tomography), a difference is observed as indicated by the stress-strain curves in Fig. 9b-d and Tables 4 and 5. Comparing the porosity values of cubic regular and cubic irregular configuration of  $\mu$ CT FE models and the experimental specimen, approximately 5% decrease in porosity is observed for experimental specimens which increases their stiffness and the yield strength. Therefore, the Young's modulus and the yield strength of  $\mu$ CT FE model tabulated in Tables 4 and 5 is lesser than the experimental values. Furthermore, when comparing the experimental and  $\mu$ CT FE model values for trabecular we see a clear overlap of the stress-strain curve despite the difference in the porosity. This is due to the random distribution of the struts and depends on the location of the selected RVE. Also, the analysis was carried out using a Multi-linear isotropic material model (MISO) discussed in section, the use of material data from bulk specimen may have a slight impact

on the difference between the  $\mu$ CT FE model and the experimental data but the major contribution is due to the difference in the porosity.

The plastic strain in the CAD as-designed models is used to predict the fracture locations in the structures as shown in Fig. 10. The failure band is at the upper region for the cubic irregular structures and is a combination of failure at junctions and at the struts. In cubic regular samples, the failure occurs exactly at the center of the strut away from the junctions in a cup and cone fashion. In trabecular structures, the failure is mostly at the junctions is randomly distributed across the sample. Comparing the FE prediction with experimental results, the failure occurs at the same location despite the decrease in the difference in porosity between as-designed and as-built porosity. Fig. 11 indicates the failure locations of the RVE models of  $\mu$ CT. In these models as well, the failure in cubic irregular samples was at the junctions and at struts mid-sections. The cubic regular samples showed failure at the mid-section of the struts while in trabecular structures the failure was primarily observed at the junctions.

In the next section, the behavior of the structures is predicted using the Gibson–Ashby model by considering the Young's modulus from experimental (tensile and compression), CAD as-designed structures (tensile and compression) and  $\mu$ CT structures (tensile).

### 3.5. Gibson–Ashby model

The Gibson–Ashby model is one of the most widely used model for cellular and lattice structures. The model expresses different properties as a function of relative density [21]. The Gibson–Ashby model for Young's modulus is as shown in equation below. The coefficient  $C$  and power  $n$  is highly dependent on the cell topology. For stretching domi-

**Table 6**  
Co-efficients of Gibson–Ashby model.

Sample	C	n	R <sup>2</sup>
Cubic Regular	0.62	1.21	0.98
Cubic Irregular	0.37	1.33	0.94
Trabecular	0.36	1.45	0.9

nated structures  $n=1$  and for bending dominated  $n=2$  [21].

$$\frac{E}{E_S} = C \left( \frac{\rho}{\rho_S} \right)^n \quad (1)$$

The variation of the relative Young's modulus with the relative density for all the samples is as shown in Fig. 12. The value of C and n form is calculated by fitting the curve using power law used in Fig. 12(a) and constants are tabulated in Table 6.

To better visualize the behavior of the samples, a log-log graph is plotted as shown in Fig. 12(b) Two linear fitting lines are used with a slope =1 for ideal stretching dominated behavior and slope =2 for ideal bending dominated behavior. It can be observed that the cubic regular structures are close to stretching dominated behavior. The cubic irregular and trabecular represent bending dominated. The points do not exactly coincide with the fitted line, several studies have concluded that the residual stresses from the LB-PBF process [52], error in calculating the relative density since loose particles do not contribute to the mechanical performance [53], and variation in the strut geometry [54]. However, the R<sup>2</sup> values from the power law indicate that the considered topologies follow the Gibson – Ashby prediction considerably well.

#### 4. Conclusion

In this study, three cell topologies were considered: cubic regular, cubic irregular and trabecular. The samples were designed to have all the same strut thickness of 200 μm and pore size of 1500 μm. LB-PBF manufacturing technique was employed by using Ti6Al4V alloy powder. The samples were subjected to tensile and compression testing under monotonic and cyclic conditions to study their mechanical response. One sample in each batch was subjected to μCT scan to study the morphological deviation of as-built samples and to reconstruct the actual geometry for FE analysis. The experimental results were compared with the FE results. The effect of relative density and cell topology is validated using the Gibson–Ashby model by considering the as-built and as-designed structures. The results from the study led to the following conclusions:

- A significant difference was observed between the as-designed and the as-built samples. The cubic regular samples had the least deviation. This is due to the well-established geometry and the strut orientation. Processing parameters and the orientation of the strut play a major role in the geometrical deviation and strut defects in the samples, which further impact on their mechanical response.
- The morphological analysis from the μCT scans indicate that the maximum surface area had a thickness in the range of 300–400 μm, while the designed thickness was 200 μm. In addition, struts parallel to the printing plane displayed higher deviation due to the effect of melt pool on unsupported surfaces.
- The monotonic and cyclic test indicated that increasing the irregularity in the structure decreased the Young's modulus and strength of the samples. The Young's moduli obtained from the cyclic tests were more consistent in both the loading conditions.
- The cyclic test indicate that the tensile samples are more stable compared to compression samples for Young's modulus measurement. However, the presence of transition in the tensile samples increased the Young's modulus under tensile loading compared to the compression loading as reported.

- Stress-strain curves derived from the μCT model better represent the experimental results compared to the as-designed structures. Nevertheless, for the accurate prediction of the experimental results, complete reconstruction of the entire tensile sample with the transition is necessary.
- Regardless of the difference in the porosity of the as-designed and as-built structures, the fracture location of the FE analysis matches with the experimental location.
- The Young's modulus obtained from the FE analyses and experiments from both the as-built and as-designed structures were used to study the effect of relative density. The Gibson–Ashby model is used to study the behavior, which indicates that the cubic regular samples were stretching dominated, while the cubic irregular and trabecular samples were bending dominated.
- The displacement of the nodes in the cubic irregular samples had a greater impact in converting the stretching dominated behavior of cubic regular samples to bending dominated. Cubic irregular has higher stiffness and strength while compared to trabecular but have similar bending dominated behavior. The stiffness values reported for all the topologies are in the range of the bone stiffness and can be considered for implant design.

#### Declaration of Competing Interest

The authors declare that they have no known competing financial interests or personal relationships that could have appeared to influence the work reported in this paper.

#### References

- [1] T.D. Ngo, A. Kashani, G. Imbalzano, et al., Additive manufacturing (3D printing): a review of materials, methods, applications and challenges, Compos. Part B Eng. 143 (2018) 172–196.
- [2] W.E. Frazier, Metal additive manufacturing: a review, J. Mater. Eng. Perform. 23 (2014) 1917–1928.
- [3] A. Bandyopadhyay, K.D. Traxel, Invited review article: metal-additive manufacturing—modeling strategies for application-optimized designs, Addit. Manuf. 22 (2018) 758–774.
- [4] T. Maconachie, M. Leary, B. Lozanovski, et al., SLM lattice structures: properties, performance, applications and challenges, Mater. Des. 183 (2019) 108137.
- [5] J.P. Kruth, G. Levy, F. Klocke, et al., Consolidation phenomena in laser and powder-bed based layered manufacturing, CIRP Ann. – Manuf. Technol. 56 (2007) 730–759.
- [6] C. Yan, L. Hao, A. Hussein, et al., Evaluations of cellular lattice structures manufactured using selective laser melting, Int. J. Mach. Tools Manuf. 62 (2012) 32–38.
- [7] M. Helou, Kara S. Design, analysis and manufacturing of lattice structures: an overview, Int. J. Comput. Integr. Manuf. 31 (2018) 243–261.
- [8] J. Banhart, Manufacture, characterisation and application of cellular metals and metal foams, Prog. Mater. Sci. 46 (2001) 559–632.
- [9] M.F. Ashby, The properties of foams and lattices, Philos. Trans. R. Soc. A Math. Phys. Eng. Sci. 364 (2006) 15–30.
- [10] A. Zargarian, M. Esfahanian, J. Kadkhodapour, et al., Numerical simulation of the fatigue behavior of additive manufactured titanium porous lattice structures, Mater. Sci. Eng. C 60 (2016) 339–347.
- [11] Mark Long, H.J. Rack, Titanium alloys in total joint replacement – a materials science perspective, Biomaterials 19 (1998) 1621–1639.
- [12] L.E. Murr, S.M. Gaytan, F. Medina, et al., Characterization of Ti-6Al-4V open cellular foams fabricated by additive manufacturing using electron beam melting, Mater. Sci. Eng. A 527 (2010) 1861–1868.
- [13] G. Ryan, A. Pandit, D.P. Apatsidis, Fabrication methods of porous metals for use in orthopaedic applications, Biomaterials 27 (2006) 2651–2670.
- [14] S. Arbabnejad Khanoki, D. Pasini, Fatigue design of a mechanically biocompatible lattice for a proof-of-concept femoral stem, J. Mech. Behav. Biomed. Mater. 22 (2013) 65–83.
- [15] S.M. Ahmadi, S.A. Yavari, R. Wauthle, et al., Additively manufactured open-cell porous biomaterials made from six different space-filling unit cells: the mechanical and morphological properties, Materials 8 (2015) 1871–1896.
- [16] M. Dallago, V. Fontanari, E. Torresani, et al., Fatigue and biological properties of Ti-6Al-4V ELI cellular structures with variously arranged cubic cells made by selective laser melting, J. Mech. Behav. Biomed. Mater. 78 (2018) 381–394.
- [17] S. Amin Yavari, S.M. Ahmadi, R. Wauthle, et al., Relationship between unit cell type and porosity and the fatigue behavior of selective laser melted meta-biomaterials, J. Mech. Behav. Biomed. Mater. 43 (2015) 91–100.
- [18] S.Y. Choy, C.N. Sun, K.F. Leong, et al., Compressive properties of functionally graded lattice structures manufactured by selective laser melting, Mater. Des. 131 (2017) 112–120.

- [19] L. Yang, R. Mertens, M. Ferrucci, et al., Continuous graded Gyroid cellular structures fabricated by selective laser melting: design, manufacturing and mechanical properties, *Mater. Des.* 162 (2019) 394–404.
- [20] C.N. Kelly, J. Francovich, S. Julmi, et al., Fatigue behavior of As-built selective laser melted titanium scaffolds with sheet-based gyroid microarchitecture for bone tissue engineering, *Acta Biomater.* 94 (2019) 610–626.
- [21] L.J. Gibson, M.F. Ashby, *Cellular Solids: Structure and Properties*, Second, Cambridge University Press, 1997 Epub ahead of print 1997, doi:10.1017/CBO9781139878326.
- [22] M. Zhang, Y. Yang, D. Wang, et al., Effect of heat treatment on the microstructure and mechanical properties of Ti6Al4V gradient structures manufactured by selective laser melting, *Mater. Sci. Eng. A* 736 (2018) 288–297.
- [23] R. Wauthle, B. Vrancken, B. Beynaerts, et al., Effects of build orientation and heat treatment on the microstructure and mechanical properties of selective laser melted Ti6Al4V lattice structures, *Addit. Manuf.* 5 (2015) 77–84.
- [24] M. Benedetti, E. Torresani, M. Leoni, et al., The effect of post-sintering treatments on the fatigue and biological behavior of Ti-6Al-4V ELI parts made by selective laser melting, *J. Mech. Behav. Biomed. Mater.* 71 (2017) 295–306.
- [25] E. Hernández-Navia, C.J. Smith, F. Dergutti, et al., The effect of defects on the mechanical response of Ti-6Al-4V cubic lattice structures fabricated by electron beam melting, *Acta Mater.* 108 (2016) 279–292.
- [26] C. Qiu, S. Yue, N.J.E. Adkins, et al., Influence of processing conditions on strut structure and compressive properties of cellular lattice structures fabricated by selective laser melting, *Mater. Sci. Eng. A* 628 (2015) 188–197.
- [27] P. Delroisse, P.J. Jacques, E. Maire, et al., Effect of strut orientation on the microstructure heterogeneities in AlSi10Mg lattices processed by selective laser melting, *Scr. Mater.* 141 (2017) 32–35.
- [28] S. Raghavendra, A. Molinari, V. Fontanari, et al., Effect of strut cross section and strut defect on tensile properties of cubic cellular structure, *Mater. Des. Process. Commun.* (2019) 1–6.
- [29] M. Dallago, B. Winiarski, F. Zanini, et al., On the effect of geometrical imperfections and defects on the fatigue strength of cellular lattice structures additively manufactured via selective laser melting, *Int. J. Fatigue* 124 (2019) 348–360.
- [30] S. Carmignato, F. Zanini, M. Baier, et al., X-ray computed tomography, in: *Precision Metal Additive Manufacturing*, CRC Press, 2020, pp. 313–346.
- [31] A. du Plessis, Effects of process parameters on porosity in laser powder bed fusion revealed by X-ray tomography, *Addit. Manuf.* 30 (2019) 100871.
- [32] S. Abrate, G. Epasto, E. Kara, et al., Computed tomography analysis of impact response of lightweight sandwich panels with micro lattice core, *Proc. Inst. Mech. Eng. Part C J. Mech. Eng. Sci.* 232 (2018) 1348–1362.
- [33] G. Epasto, G. Palomba, D. D'Andrea, et al., Ti-6Al-4V ELI microlattice structures manufactured by electron beam melting: effect of unit cell dimensions and morphology on mechanical behaviour, *Mater. Sci. Eng. A* 753 (2019) 31–41.
- [34] A.E. Wilson-Heid, T.C. Novak, A.M. Beese, Characterization of the effects of internal pores on tensile properties of additively manufactured austenitic stainless steel 316L, *Exp. Mech.* 59 (2019) 793–804.
- [35] B. Lozanovski, M. Leary, P. Tran, et al., Computational modelling of strut defects in SLM manufactured lattice structures, *Mater. Des.* 171 (2019) 107671.
- [36] S. Van Bael, G. Kerckhofs, M. Moesen, et al., Micro-CT-based improvement of geometrical and mechanical controllability of selective laser melted Ti6Al4V porous structures, *Mater. Sci. Eng. A* 528 (2011) 7423–7431.
- [37] C. Petit, E. Maire, S. Meille, et al., CoCrMo cellular structures made by electron beam melting studied by local tomography and finite element modelling, *Mater. Charact.* 116 (2016) 48–54.
- [38] N. Michailidis, F. Stergioudi, H. Omar, et al., Experimental and FEM analysis of the material response of porous metals imposed to mechanical loading, *Colloids Surf. A Physicochem. Eng. Asp.* 382 (2011) 124–131.
- [39] Y. Amani, S. Dancette, P. Delroisse, et al., Compression behavior of lattice structures produced by selective laser melting: x-ray tomography based experimental and finite element approaches, *Acta Mater.* 159 (2018) 395–407.
- [40] U.E. Pazzaglia, F. Ghisellini, D. Barbieri, et al., Failure of the stem in total hip replacement – a study of aetiology and mechanism of failure in 13 cases, *Arch. Orthop. Trauma Surg.* 107 (1988) 195–202.
- [41] T.P. Andriacchi, J.O. Galante, T. Belytschko, et al., A stress analysis of the femoral stem in total hip prostheses, *J. Bone Joint Surg. Am.* 58 (5) (1976) 618–624.
- [42] S. Raghavendra, A. Molinari, V. Fontanari, et al., Tension-compression asymmetric mechanical behaviour of lattice cellular structures produced by selective laser melting, *Proc. Inst. Mech. Eng. Part C J. Mech. Eng. Sci.* (2020) 095440622091278.
- [43] S. Carmignato, W. Dewulf, R. Leach (Eds.), *Industrial X-Ray Computed Tomography* Springer International Publishing, Cham, 2018 Epub Ahead of Print, doi:10.1007/978-3-319-59573-3.
- [44] A. Cuadrado, A. Yáñez, O. Martel, et al., Influence of load orientation and of types of loads on the mechanical properties of porous Ti6Al4V biomaterials, *Mater. Des.* 135 (2017) 309–318.
- [45] E. Brun, J. Vicente, F. Topin, et al., Microstructure and transport properties of cellular materials: representative volume element, *Adv. Eng. Mater.* 11 (2009) 805–810.
- [46] S. Youssef, E. Maire, R. Gaertner, Finite element modelling of the actual structure of cellular materials determined by X-ray tomography, *Acta Mater.* 53 (2005) 719–730.
- [47] J. Yang, H. Yu, J. Yin, et al., Formation and control of martensite in Ti-6Al-4V alloy produced by selective laser melting, *Mater. Des.* 108 (2016) 308–318.
- [48] F. Zanini, E. Sbettega, S. Carmignato, X-ray computed tomography for metal additive manufacturing: challenges and solutions for accuracy enhancement, *Procedia CIRP* 75 (2018) 114–118.
- [49] J. Parthasarathy, B. Starly, S. Raman, et al., Mechanical evaluation of porous titanium (Ti6Al4V) structures with electron beam melting (EBM), *J. Mech. Behav. Biomed. Mater.* 3 (2010) 249–259.
- [50] M. Dallago, B. Winiarski, F. Zanini, et al., On the effect of geometrical imperfections and defects on the fatigue strength of cellular lattice structures additively manufactured via selective laser melting, *Int. J. Fatigue* 124 (2019) 348–360.
- [51] C. Peng, P. Tran, H. Nguyen-Xuan, et al., Mechanical performance and fatigue life prediction of lattice structures: parametric computational approach, *Compos. Struct.* 235 (2020) 111821.
- [52] C. Yan, L. Hao, A. Hussein, et al., Advanced lightweight 316L stainless steel cellular lattice structures fabricated via selective laser melting, *Mater. Des.* 55 (2014) 533–541.
- [53] A.A. Zadpoor, Mechanical performance of additively manufactured meta-biomaterials, *Acta Biomater.* 85 (2019) 41–59.
- [54] X.Z. Zhang, M. Leary, H.P. Tang, et al., Selective electron beam manufactured Ti-6Al-4V lattice structures for orthopedic implant applications: current status and outstanding challenges, *Curr. Opin. Solid State Mater. Sci.* 22 (2018) 75–99.